IOP Publishing Smart Materials and Structures
Smart Mater. Struct. 24 (2015) 045031 (19pp) doi:10.1088/0964-1726/24/4/045031

Thermo-mechanically coupled fracture analysis of shape memory alloys using the extended finite element method

S Hatefi Ardakani, H Ahmadian and S Mohammadi[1]

High Performance Computing Laboratory, School of Civil Engineering, University of Tehran, Tehran, Iran

E-mail: s.hatefi@ut.ac.ir, h.ahmadian@ut.ac.ir and smoham@ut.ac.ir

Received 30 August 2014, revised 1 February 2015
Accepted for publication 9 February 2015
Published 3 March 2015

Abstract

In this paper, the extended finite element method is used for fracture analysis of shape memory alloys for both cases of super elastic and shape memory effects. Heat generation during the forward and reverse phase transformations can lead to temperature variation in the material because of strong thermo-mechanical coupling, which significantly influences the SMA mechanical behavior. First, the stationary crack mode is studied and the effects of loading rate on material behavior in the crack tip are examined. Then, the crack propagation analysis is performed in the presence of an initial crack by adopting a weighted averaging criterion, where the direction of crack propagation is determined by weighted averaging of effective stresses at all the integration points in the vicinity of the crack tip. Finally, several numerical examples are analyzed and the obtained results are compared with the available reference results.

Keywords: shape memory alloys (SMAs), extended finite element method (XFEM), thermo-mechanical coupling, crack propagation

(Some figures may appear in colour only in the online journal)

1. Introduction

Shape memory alloys (SMAs) are among the growing state of the art smart materials that are being increasingly used in various sensitive engineering applications owing to the possession of two very important properties: super elasticity and shape memory effect (SME) [1]. As typically illustrated in figure 1(a), in temperatures greater than A_f, SMA is in the stable austenite phase. By applying a mechanical load it transforms into the martensite phase and since it needs to retrieve its stable phase, it transforms back to the austenite phase after unloading, representing the super elastic behavior. When the temperature is lower than A_s, no reverse transformation occurs after unloading. But, if the temperature is increased to a level greater than A_f, a reverse phase transformation occurs, which is called the SME. Figure 1(b) schematically shows the stress–strain curves for super elastic and SME behaviors. M_s and M_f are the martensite transformation start and finish temperatures, and A_f and A_f represent the austenite transformation start and finish temperatures, respectively. Also, σ_{M_s} and σ_{A_s} are the start stresses of forward and reverse transformations, and σ_{M_f} and σ_{A_f} define the finish ones, respectively. There are, however, other attitudes towards the terminologies being used in this subject. For further discussion see [1–3].

Generally, research on SMAs could be classified into three categories: small scales such as microstructure studies, continuum level analysis and the failure simulations, which is the subject of the present paper. Compared to other types of materials, SMAs exhibit more complicated failure mechanisms due to localized phase transformations at the crack tip which directly affect the process zone. The conventional theory of fracture mechanics cannot be directly applied for SMAs, due to the fact that substantial phase transformation occurs at the crack tip which affects the nearby stress field. Figure 2 typically illustrates the phase transformation regions and stress distribution around the crack tip in an SMA. In the region near to the crack tip, the phase is martensite (M). A little far from the crack tip, the phase transformation ($A \rightarrow M$)

[1] Author to whom any correspondence should be addressed.

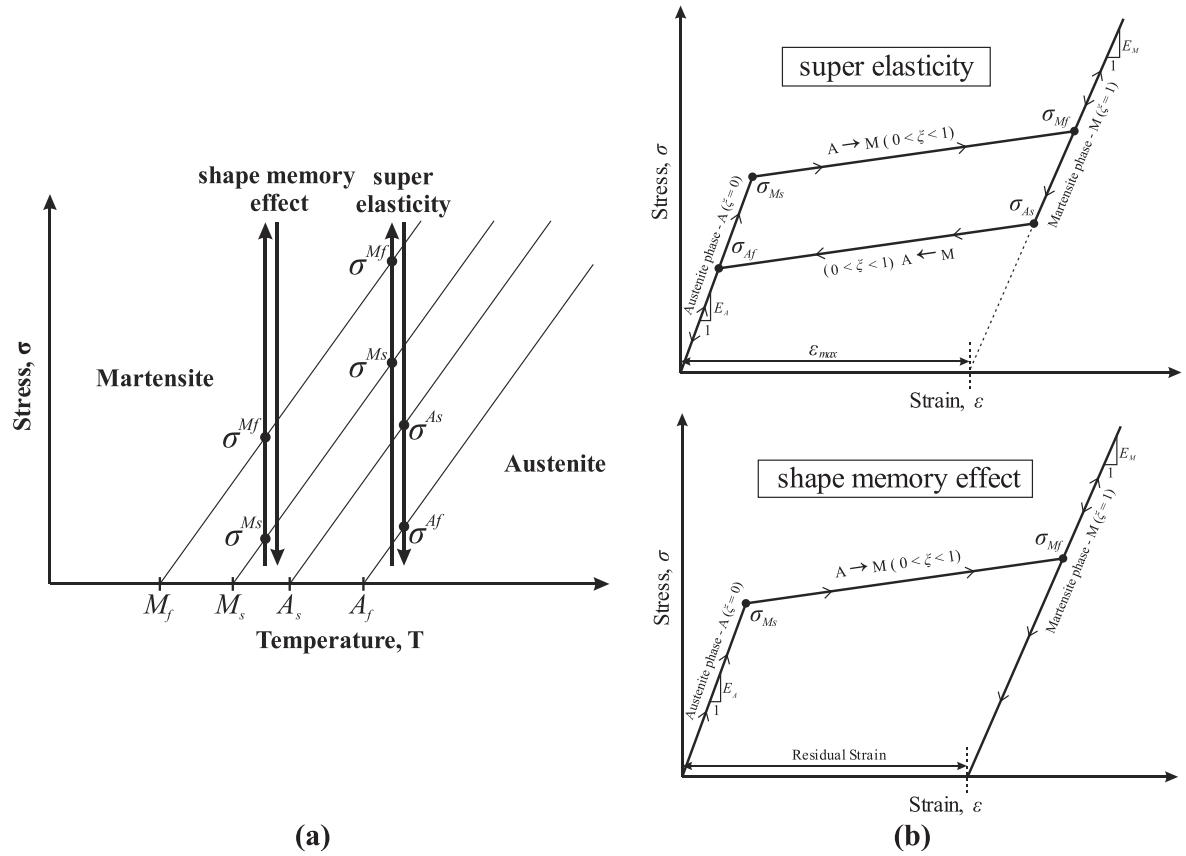

Figure 1. Typical loading paths and stress–strain curves for super elastic and shape memory effects (a) loading paths, (b) stress–strain curves.

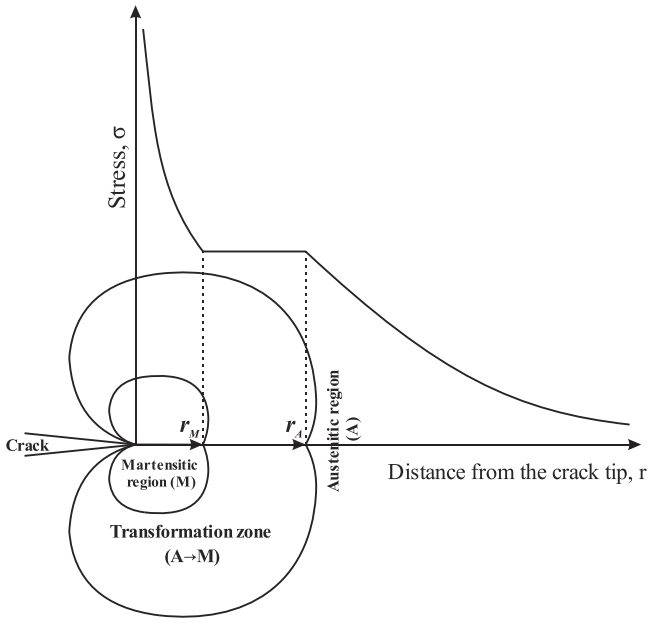

Figure 2. Typical stress distribution and phase transformation regions near the crack tip in an SMA.

occurs, whereas further away from this region no phase transformation occurs and the phase remains austenite (*A*).

A variety of experimental, analytical and numerical studies have been performed to study the fracture behavior of SMAs. The experimental studies were conducted for examining how the crack creation and propagation under monotonic and cyclic loadings [4–7]. The analytical studies were carried out for determination of the stress field and the size of the phase transformation region [8–11]. Birman [8] presented an estimation for the size of phase transformation regions by improving the available classical relations for the size of the plastic zone around the crack tip in conventional engineering materials. Yi and Gao [11] concluded that the phase transformation could decrease the stress intensity factor and would lead to toughening in the crack tip. Maletta and Furgiuele [10] provided an analytical model for investigation of the forward phase transformation in the crack tip by assuming a constant stress through the phase transformation. Furthermore, Maletta [12] considered the effects of tri-linear stress–strain response of SMAs and analytically formulated the stress fields and determined the size of the transformation regions near the crack tip of SMAs without the assumption of constant stress through the phase transformation process. Desindes and Daly [9] developed a model for determining the shape of the phase transformation regions only for the mode III crack.

In addition to the experimental and analytical studies, several numerical studies have been performed for investigation of the phase transformation effect on the material behavior in the crack tip considering the thermodynamic parameters and different loading conditions by using the finite element method [13–15]. Also, Freed and Banks-Sills presented a cohesive crack model for more accurate evaluation of

forward and reverse phase transformations with crack propagation [2]. Proposing a cohesive crack model, Baxevanis and Lagoudas investigated the effects of different phase transformation characteristics such as the maximum transformation strain on fracture behavior and evaluated the sizes of transformed zones at the crack tip of SMAs [16]. Moreover, Baxevanis *et al* studied the propagation of mode I crack in SMAs using a virtual crack closure technique considering the effects of plasticity of martensite phase [17].

Despite the considerable developments of the finite element method, the boundary element technique and a variety of meshless methods for solving crack problems [18–20], the extended finite element method (XFEM) has proved to be a very powerful tool for modeling general weak and strong discontinuity problems. The main idea of XFEM is based on adding the discontinuous functions to the displacement field approximation of the cracked elements. The XFEM procedure allows for crack propagation problems to be simulated without any remeshing. Since its introduction [21], XFEM has been applied for modeling a wide range of new problems in solid mechanics such as modeling of shear bands [22, 23], thermo-mechanical fracture analysis of FGMs [24–26], brittle [27, 28] and ductile [29, 30] crack modelings, and static and dynamic fracture analysis of orthotropic media [31–34].

The main purpose of this research is to study the thermo–mechanical coupling fracture of SMAs using XFEM. Despite the fact that it is possible to analyze the cracking of SMA in the unstable phase transformation case by using the softening model of Ahmadian *et al* [35], in this paper, it is assumed that the initial unstable behavior of SMA is shaken out by a cyclical training and the behavior is completely stable, and a hardening model is assumed for the transformation region. This paper is organized as follows: first, the adopted constitutive model of SMA is presented. Then, solution of the thermo–mechanical coupling problem in the framework of XFEM is presented in section 3. It also discusses brief descriptions of the XFEM model to deal with cracks in SMA and crack propagation criterion. Several numerical examples, in two cases of stationary and progressive cracks, are then investigated and the results are compared with the available reference results.

2. Constitutive model

The constitutive model, presented by Boyd and Lagoudas [36] based on the Gibbs free energy G is adopted

$$G = -\frac{1}{2\rho}\boldsymbol{\sigma}\colon \boldsymbol{C}\colon \boldsymbol{\sigma} - \frac{1}{\rho}\boldsymbol{\sigma}\colon \left[\boldsymbol{\alpha}\left(T - T_0\right) + \boldsymbol{\varepsilon}^{\mathrm{tr}}\right] + c\left[\left(T - T_0\right) - T\ln\left(\frac{T}{T_0}\right)\right] - s_0 T + u_0 + \frac{1}{\rho}f(\xi), \quad (1)$$

where $\boldsymbol{C}$ denotes the effective compliance tensor, $\boldsymbol{\sigma}$ is the stress tensor, $\boldsymbol{\varepsilon}^{\mathrm{tr}}$ represents the transformation strain and $\boldsymbol{\alpha}$ is the effective thermal expansion tensor. ξ is the martensitic volume fraction which varies between 0 (fully austenitic state) and 1 (fully martensitic state). T and T_0 are the current and reference temperatures, respectively. ρ is the density, c represents the effective specific heat, and u_0 and s_0 are the effective specific internal energy and the effective specific entropy at the reference state, respectively. f is the hardening function which will be defined in the following section.

The strain tensor $\boldsymbol{\varepsilon}$ can be defined in terms of $\boldsymbol{\sigma}$

$$\boldsymbol{\varepsilon} = \boldsymbol{C}\colon \boldsymbol{\sigma} + \boldsymbol{\alpha}\left(T - T_0\right) + \boldsymbol{\varepsilon}^{\mathrm{tr}}. \quad (2)$$

Considering the nonlinear behavior of SMA during forward and reverse transformations and its similarity to plasticity, equation (3) governs the relation between $\boldsymbol{\varepsilon}^{\mathrm{tr}}$ and ξ

$$\dot{\boldsymbol{\varepsilon}}^{\mathrm{tr}} = \boldsymbol{\Lambda}\dot{\xi}. \quad (3)$$

$\boldsymbol{\Lambda}$ is the transformation tensor

$$\boldsymbol{\Lambda} = \begin{cases} \dfrac{3}{2}\varepsilon_{\max}\dfrac{\boldsymbol{\sigma}'}{\bar{\sigma}'}; & \dot{\xi} > 0 (A \to M), \\ \varepsilon_{\max}\dfrac{\boldsymbol{\varepsilon}^{\mathrm{tr}-R}}{\bar{\varepsilon}^{\mathrm{tr}-R}}; & \dot{\xi} < 0 (M \to A), \end{cases} \quad (4)$$

$$\bar{\sigma}' = \sqrt{\frac{3}{2}}\,\|\boldsymbol{\sigma}'\|, \quad (5)$$

$$\bar{\varepsilon}^{\mathrm{tr}-R} = \sqrt{\frac{2}{3}}\,\left\|\boldsymbol{\varepsilon}^{\mathrm{tr}-R}\right\|, \quad (6)$$

where $\varepsilon_{\max}$ is the material parameter related to the maximum uniaxial transformation strain, $\boldsymbol{\sigma}'$ is the deviatoric stress tensor and $\boldsymbol{\varepsilon}^{\mathrm{tr}-R}$ is the transformation strain at the reversal point. $\bar{\sigma}'$ is the effective stress (von Mises equivalent stress) and $\bar{\varepsilon}^{\mathrm{tr}-R}$ is the effective transformation strain. In equation (4), $\dot{\xi} > 0$ and $\dot{\xi} < 0$ are related to the forward and reverse phase transformations, respectively.

For solving the nonlinear equation (3), the closest point projection return mapping algorithm is adopted [3]. The first and second law of thermodynamics can be represented in the Clausius–Planck inequality as [1]

$$\left(\boldsymbol{\sigma}\colon \boldsymbol{\Lambda} - \rho\frac{\partial G}{\partial \xi}\right)\dot{\xi} = \pi\dot{\xi} \geqslant 0. \quad (7)$$

Here, π is the thermodynamics force which can be obtained by substituting the Gibbs free energy (1) in (7):

$$\pi = \boldsymbol{\sigma}\colon \boldsymbol{\Lambda} + \frac{1}{2}\boldsymbol{\sigma}\colon \Delta\boldsymbol{C}\colon \boldsymbol{\sigma} + \boldsymbol{\sigma}\colon \Delta\boldsymbol{\alpha}\left(T - T_0\right) - \rho\Delta c\left[\left(T - T_0\right) - T\ln\left(\frac{T}{T_0}\right)\right] + \rho\Delta s_0 T - \rho\Delta u_0 - \frac{\partial f(\xi)}{\partial \xi}. \quad (8)$$

The transformation surface $\Phi^{\mathrm{tr}} = 0$ can then be defined for the forward and reverse phase transformations by reaching π to a critical value

$$\Phi^{\mathrm{tr}} = \begin{cases} \pi - Y^{\mathrm{tr}}; & \dot{\xi} > 0, \\ -\pi - Y^{\mathrm{tr}}; & \dot{\xi} < 0, \end{cases} \quad (9)$$

where Y^{tr} is the material parameter.

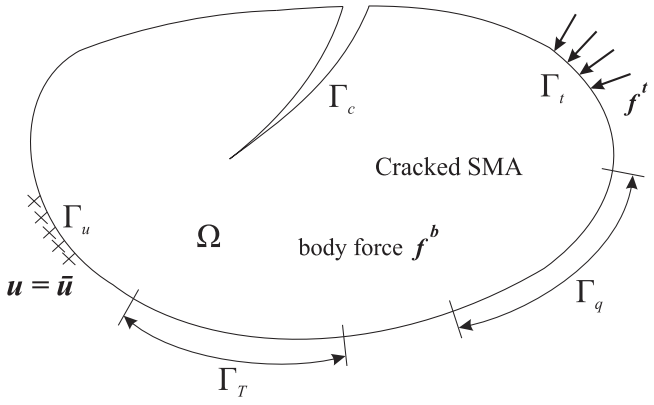

Figure 3. A typical cracked SMA.

The effective material properties c, s_0, u_0, $\boldsymbol{\alpha}$ and $\boldsymbol{C}$ can now be written in terms of ξ

$$\begin{aligned} c(\xi) &= c^{\mathbf{A}} + \xi\Delta c, \\ s_0(\xi) &= {s_0}^{\mathbf{A}} + \xi\Delta s_0, \\ u_0(\xi) &= {u_0}^{\mathbf{A}} + \xi\Delta u_0, \\ \boldsymbol{\alpha}(\xi) &= \boldsymbol{\alpha}^{\mathbf{A}} + \xi\Delta\boldsymbol{\alpha}, \\ \boldsymbol{C}(\xi) &= \boldsymbol{C}^{\mathbf{A}} + \xi\Delta\boldsymbol{C}. \end{aligned} \tag{10}$$

The hardening function $f(\xi)$ is defined for the forward and reverse phase transformations as [1]

$$f(\xi) = \begin{cases} \frac{1}{2}\rho b^M \xi^2 + \left(\mu_1 + \mu_2\right)\xi; & \dot{\xi} > 0, \\ \frac{1}{2}\rho b^A \xi^2 + (\mu_1 - \mu_2)\xi; & \dot{\xi} < 0, \end{cases} \tag{11}$$

where b^M, b^A, μ_1 and μ_2 are the material parameters.

So far, five unknown material parameters b^M, b^A, μ_1, μ_2 and Y^{tr} have to be determined, which require the following five independent equations, as comprehensively discussed in [1]

$$\begin{cases} b^M = -\Delta s_0\left(M_{\mathrm{s}} - M_{\mathrm{f}}\right), \\ b^A = -\Delta s_0\left(A_{\mathrm{f}} - A_{\mathrm{s}}\right), \\ \mu_1 = \frac{1}{2}\rho\Delta s_0\left(M_{\mathrm{s}} + A_{\mathrm{f}}\right) - \rho\Delta u_0, \\ \mu_2 = \frac{1}{4}\rho\Delta s_0\left(A_{\mathrm{s}} - A_{\mathrm{f}} - M_{\mathrm{f}} + M_{\mathrm{s}}\right), \\ Y^{\mathrm{tr}} = \frac{1}{4}\rho\Delta s_0\left(M_{\mathrm{s}} + M_{\mathrm{f}} - A_{\mathrm{f}} - A_{\mathrm{s}}\right). \end{cases} \tag{12}$$

3. Thermo–mechanical coupling

An SMA domain Ω which contains a traction-free crack is considered, as depicted in figure 3. Γ_{c} is the boundary of the crack, and Γ_t and Γ_u are the boundaries with prescribed traction $\boldsymbol{f^t}$ and displacement $\bar{\boldsymbol{u}}$, respectively. For fracture analysis, the coupling equations have to be solved. A semi-coupled iterative algorithm is applied for solving the thermo-mechanical problem by decoupling it into two parts. In each step, first the mechanical problem is solved isothermally by using XFEM and then, the temperature variations due to phase transformation can be calculated from the heat equation. The procedure continues until a certain convergence criterion is met.

3.1. The XFEM

The XFEM has become one of the main numerical tools for effective simulation of discontinuities over the past decade [21, 37, 38]. XFEM is capable of crack propagation analysis without any expensive remeshing procedures by only adding some additional degrees of freedom to the original standard finite element mesh (generated for the uncracked domain).

To simplify the process of SMA crack propagation simulation, the singularity of crack tip is disregarded in this research, and only the discontinuity across crack surfaces is considered. Addition of the crack tip singularity effects requires extensive numerical procedures to ensure stability of the complex phenomena of phase transformation and moving crack tip singular fields, which will be dealt with in an independent study. Therefore, the XFEM enriched displacement approximation for a typical point $\boldsymbol{x}$ of the domain can be written as

$$\boldsymbol{u}(\boldsymbol{x}) = \underbrace{\sum_i \phi_i(\boldsymbol{x})\boldsymbol{u}_i}_{1} + \underbrace{\sum_j \phi_j(\boldsymbol{x})\Big(H(\boldsymbol{x}) - H(\boldsymbol{x}_j)\Big)\boldsymbol{a}_j}_{2}, \tag{13}$$

where $\boldsymbol{u}$ is the nodal displacement, $\boldsymbol{a}$ is the vector of enriched nodal variables and ϕ is the shape function of the standard finite element. The heaviside function $H(\boldsymbol{x})$ for representing a discontinuous field, such as displacements across a crack, can be written as:

$$H(\boldsymbol{x}) = \begin{cases} +1, & (\boldsymbol{x} - \boldsymbol{x}^*).\,\boldsymbol{n}_{\mathrm{c}} > 0, \\ -1, & (\boldsymbol{x} - \boldsymbol{x}^*).\,\boldsymbol{n}_{\mathrm{c}} < 0, \end{cases} \tag{14}$$

where $\boldsymbol{x}^*$ is the projection of point $\boldsymbol{x}$ on Γ_{c} and $\boldsymbol{n}_{\mathrm{c}}$ is the normal vector to Γ_{c} in the point $\boldsymbol{x}^*$. For further details see [38].

The equilibrium and boundary conditions for the mechanical problem are defined as

$$\nabla.\,\boldsymbol{\sigma} + \boldsymbol{f^b} = 0, \qquad \text{in } \Omega, \tag{15}$$

$$\boldsymbol{\sigma}.\,\boldsymbol{n}_t = \boldsymbol{f^t}, \qquad \text{on } \Gamma_t, \tag{16}$$

$$\boldsymbol{u} = \bar{\boldsymbol{u}}, \qquad \text{on } \Gamma_u, \tag{17}$$

where $\boldsymbol{n}_t$ is a unit normal vector on the boundary Γ_t and $\boldsymbol{f^b}$ is the body force. Since the problem is nonlinear, the Newton–Raphson method is applied for solving the equilibrium equation incrementally. Applying the XFEM discretization procedure to the incremental form of equation (15) leads to

$$\boldsymbol{K}\Delta\boldsymbol{u}^h = \boldsymbol{f}^{\mathrm{ext}} - \boldsymbol{f}^{\mathrm{int}}, \tag{18}$$

where $\boldsymbol{u}^h$ is the displacement vector (including the standard degrees of freedom ($\boldsymbol{u}$) and enriched degrees of freedom ($\boldsymbol{a}$)) [38]

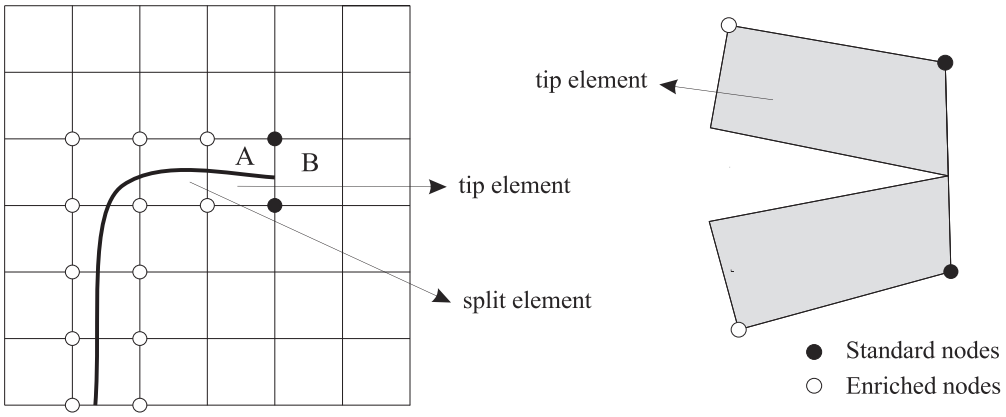

Figure 4. Selecting the nodes for enrichment with the heaviside function.

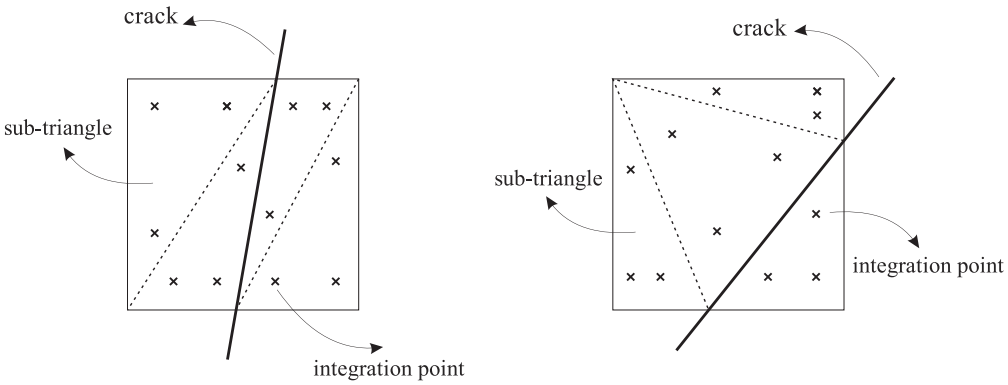

Figure 5. Subdividing the cracked elements into sub-triangles, and their associated integration points.

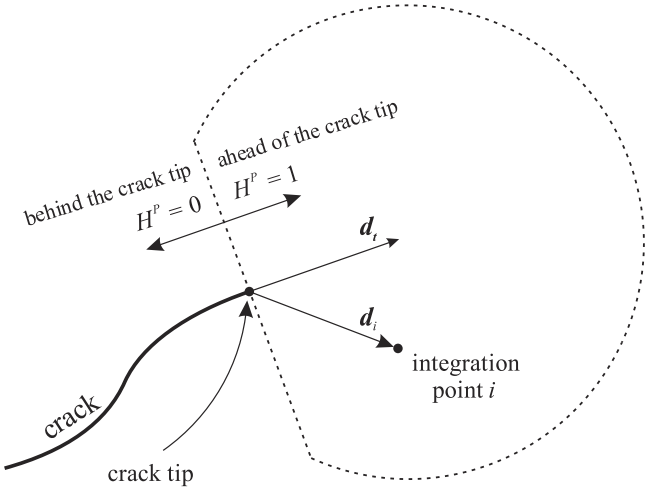

Figure 6. Calculating the direction of crack propagation.

$$\boldsymbol{u}^h = \{\boldsymbol{u} \quad \boldsymbol{a}\}^T. \tag{19}$$

In equation (18), $\boldsymbol{K}$ is the global stiffness matrix, and $\boldsymbol{f}^{\text{ext}}$ and $\boldsymbol{f}^{\text{int}}$ are the global external and internal force vectors, respectively. All terms are obtained by the assembly of the stiffness matrix and force vector of each element

$$\boldsymbol{K}_{ij}^e = \begin{bmatrix} \boldsymbol{K}_{ij}^{uu} & \boldsymbol{K}_{ij}^{ua} \\ \boldsymbol{K}_{ij}^{au} & \boldsymbol{K}_{ij}^{aa} \end{bmatrix}, \tag{20}$$

$$\left(\boldsymbol{f}_{\text{i}}^{\text{ext}}\right)^e = \left\{ \left(\boldsymbol{f}_i^{\text{ext}}\right)^u \quad \left(\boldsymbol{f}_i^{\text{ext}}\right)^a \right\}^T, \tag{21}$$

$$\left(\boldsymbol{f}_i^{\text{int}}\right)^e = \left\{ \left(\boldsymbol{f}_i^{\text{int}}\right)^u \quad \left(\boldsymbol{f}_i^{\text{int}}\right)^a \right\}^T, \tag{22}$$

where

$$\boldsymbol{K}_{ij}^{\text{pr}} = \int_{\Omega^e} \left(\boldsymbol{B}_i^p\right)^T \left(\boldsymbol{C}^A + \xi \Delta \boldsymbol{C}\right)^{-1} \boldsymbol{B}_j^r \, \mathrm{d}\Omega, \ (p, r = u, a), \tag{23}$$

$$\left(\boldsymbol{f}_i^{\text{ext}}\right)^u = \int_{\Gamma_t} \phi_i \boldsymbol{f}^t \, \mathrm{d}\Gamma + \int_{\Omega^e} \phi_i \boldsymbol{f}^b \, \mathrm{d}\Omega, \tag{24}$$

$$\left(\boldsymbol{f}_i^{\text{ext}}\right)^a = \int_{\Gamma_t} \phi_i \left(H - H_i\right) \boldsymbol{f}^t \, \mathrm{d}\Gamma + \int_{\Omega^e} \phi_i \left(H - H_i\right) \boldsymbol{f}^b \, \mathrm{d}\Omega, \tag{25}$$

$$\left(\boldsymbol{f}_i^{\text{int}}\right)^u = \int_{\Omega^e} \left(\boldsymbol{B}_i^u\right)^T \boldsymbol{\sigma} \mathrm{d}\Omega, \tag{26}$$

$$\left(\boldsymbol{f}_i^{\text{int}}\right)^a = \int_{\Omega^e} \left(\boldsymbol{B}_i^a\right)^T \boldsymbol{\sigma} \mathrm{d}\Omega, \tag{27}$$

$$\boldsymbol{B}_i^u = \begin{bmatrix} \phi_{i,x} & 0 \\ 0 & \phi_{i,y} \\ \phi_{i,y} & \phi_{i,x} \end{bmatrix}, \tag{28}$$

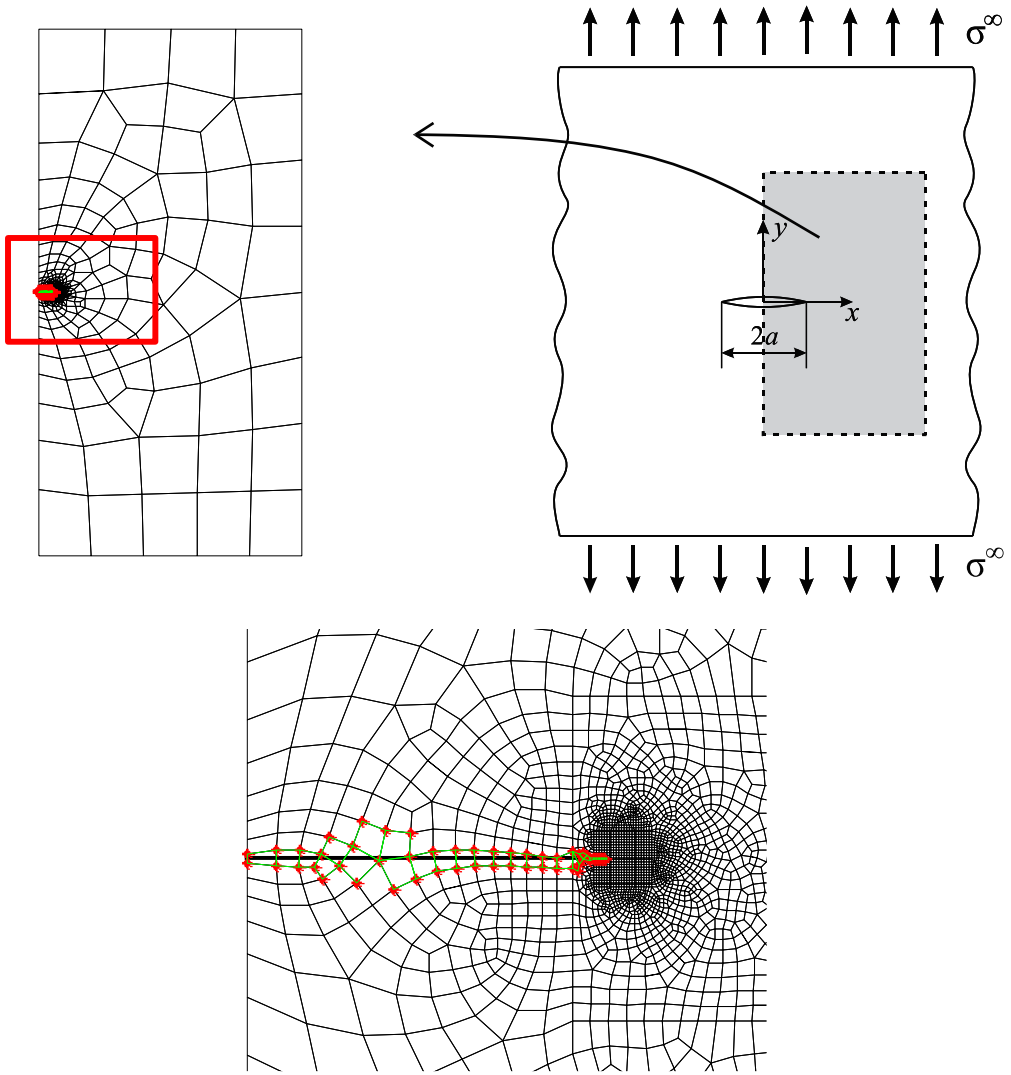

Figure 7. Details of the infinite SMA plate with a central crack, and the finite element mesh.

Table 1. Material properties of infinite SMA plate.

E_A	50.0×10^9 Pa	$C_A = C_M$	10×10^6 Pa/K
E_M	25.0×10^9 Pa	$\varepsilon_{\max}$	0.01
$\nu_A = \nu_M$	0.3	k	18.3 W/(mK)
$\rho c_A = \rho c_M$	3.2×10^5 J/(m^{3}K)	h_{Air}	4 W/(m^{2}K)
σ^{tr}=100 MPa: M_s	15 °C	σ^{tr}=200 MPa: M_s	5 °C
M_f	15 °C	M_f	5 °C
A_s	20 °C	A_s	15 °C
A_f	20 °C	A_f	15 °C

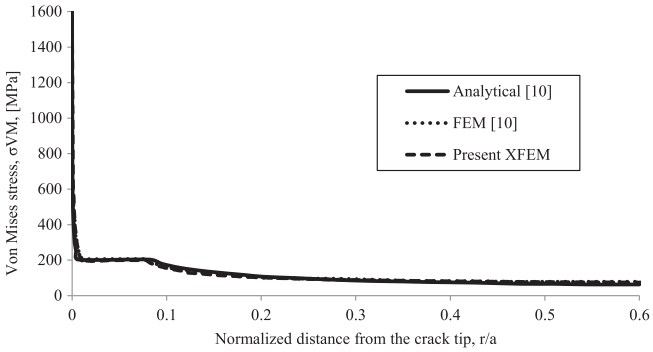

Figure 8. Predictions of the von Mises stress in the horizontal direction from the crack tip, for $\varepsilon_{\max} = 0.01$, $\sigma^{tr} = 200$ MPa and $\sigma^{\infty} = 62.5$ MPa.

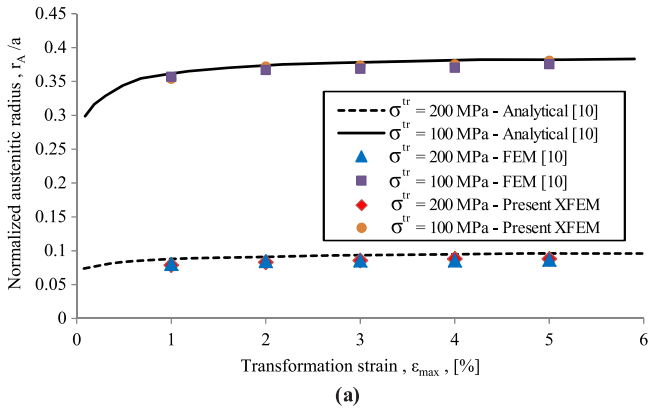

(a)

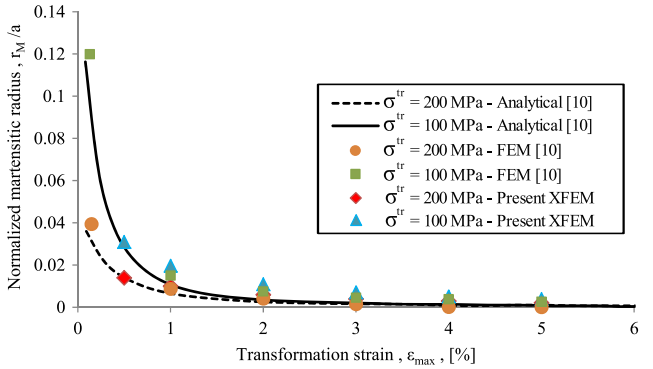

(b)

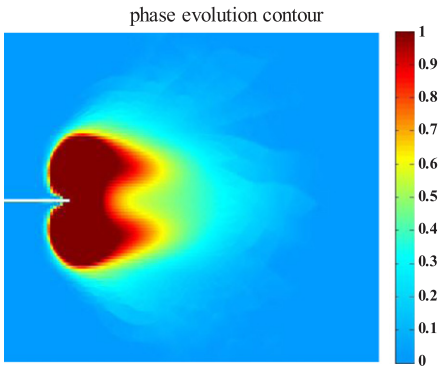

(c)

Figure 9. Size of the phase transformation regions (a) r_A/a versus $\varepsilon_{\max}$, (b) r_M/a versus $\varepsilon_{\max}$, (c) phase evolution contour in the crack tip.

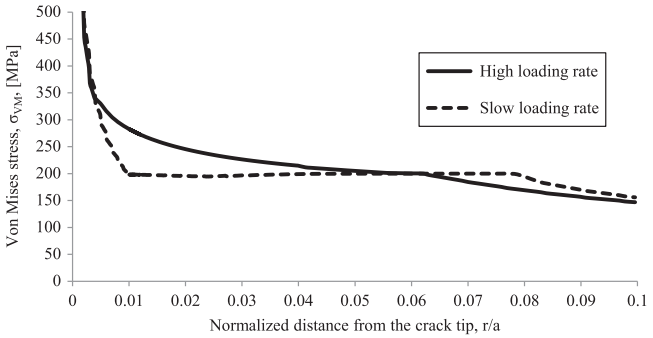

Figure 10. Prediction of the von Mises stress in the horizontal direction from the crack tip for the two cases of slow and high loading rates.

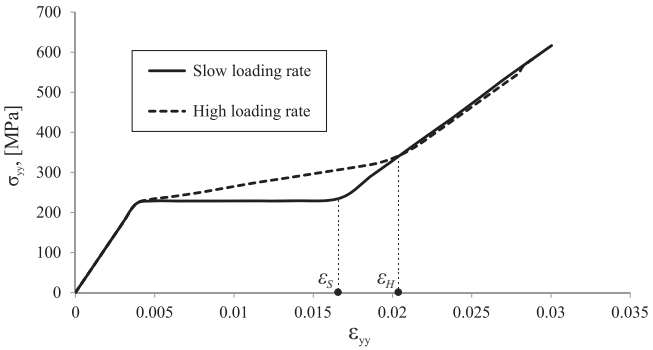

Figure 11. Local stress–strain curve ($\sigma_{yy} - \varepsilon_{yy}$) in an integration point in front of the crack tip for two cases of slow and high loading rates.

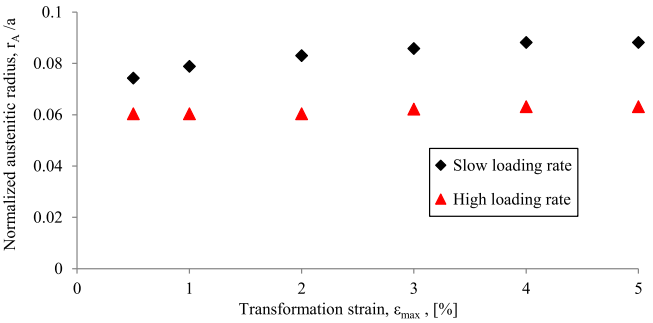

(a)

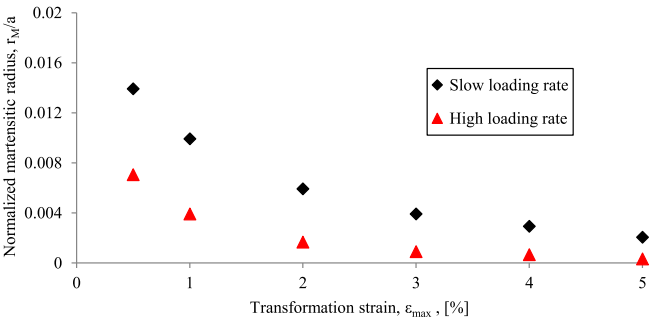

(b)

Figure 12. Comparison between the sizes r_A and r_M of phase transformation regions for two cases of slow and fast loading rates with $\sigma^{tr} = 200$ MPa.

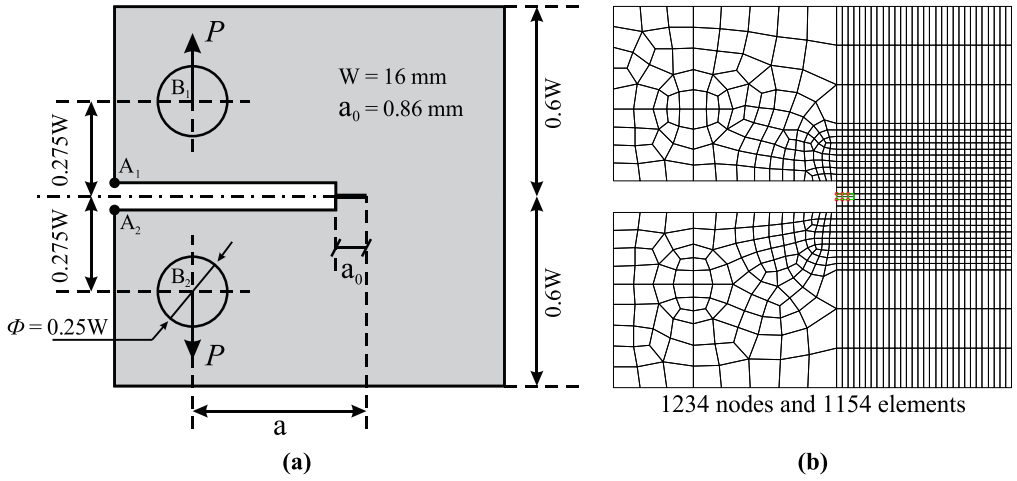

Figure 13. Geometric details and the finite element mesh of the compact tension test.

Table 2. Material properties of SMA specimen.

E_M	8.22×10^9 Pa	$C_A = C_M$	10×10^6 Pa K^{-1}
E_A	56.5×10^9 Pa	$\varepsilon_{\max}$	0.0048
$\nu_A = \nu_M$	0.33	k	18.3 W (m K)$^{-1}$
M_s	−31 °C	h_{Air}	4 W (m^{2}K)$^{-1}$
M_f	−34 °C	$(\sigma_{\text{crit}})_{\text{superelastic}}$	728 MPa
A_s	−8.5 °C	$(\sigma_{\text{crit}})_{\text{SME}}$	400 MPa
A_f	4 °C		

Table 3. Definition of the loading types.

Loading rates	Description
Coupled—$2 \times 10^{+1}$ mm s^{-1}	High loading rate
Coupled—2×10^{-1} mm s^{-1}	—
Coupled—2×10^{-2} mm s^{-1}	—
Coupled—2×10^{-3} mm s^{-1}	Very slow loading rate (near isothermal)
Uncoupled	Isothermal

$$\boldsymbol{B}_i^a = \begin{bmatrix} \left(\phi_i(H - H_i)\right)_{,x} & 0 \\ 0 & \left(\phi_i(H - H_i)\right)_{,y} \\ \left(\phi_i(H - H_i)\right)_{,y} & \left(\phi_i(H - H_i)\right)_{,x} \end{bmatrix}, \tag{29}$$

where $\boldsymbol{B}$ is the matrix of shape function derivatives.

3.2. Solving the coupled heat equation

Assuming that the effective specific heat and the thermal expansion coefficients have the same value for both phases (A and M), the fully coupled heat equation of SMA is written as [1]

$$T\boldsymbol{\alpha}\colon \dot{\boldsymbol{\sigma}} + \rho c\dot{T} + \left(-\pi + \rho\Delta s_0 T\right)\dot{\xi} = -\nabla .\ q, \tag{30}$$

where q is the heat flux.

The essential and convective boundary conditions and initial values associated with this heat equation are as follows:

$$\left.\begin{aligned} &T = T_0 \quad \text{on } \Gamma_T \\ &q.\ n_q = h\left(T - T_0\right) \quad \text{on } \Gamma_q \end{aligned}\right\} \rightarrow \text{boundary conditions},$$
$$\left.\begin{aligned} &T(t = 0) = T_0 \end{aligned}\right\} \rightarrow \text{initial condition}, \tag{31}$$

where Γ_T and Γ_q are the boundaries where the temperature (essential) and convective boundary conditions are applied, respectively. n_q is the normal vector to the boundary Γ_q and t is the time. Assuming the heat conduction to follow the Fourier's law, $q = -k\nabla T$, the heat equation is written as

$$T\boldsymbol{\alpha}\colon \dot{\boldsymbol{\sigma}} + \rho c\dot{T} + \left(-\pi + \rho\Delta s_0 T\right)\dot{\xi} = \nabla .\ (k\nabla T). \tag{32}$$

Applying the conventional finite element discretization and assuming that the problem is solved in a semi transient state, the heat equation can be written in the following incremental form

$$\boldsymbol{K}_{\text{eq}}{}^{n+1}\boldsymbol{T}^{n+1} = \boldsymbol{F}_{\text{eq}}{}^{n+1}, \tag{33}$$

where

$$\left.\begin{aligned} \boldsymbol{K}_{\text{eq}}{}^{n+1} &= \left(\boldsymbol{K}_k + \boldsymbol{K}_h + \boldsymbol{K}_\sigma{}^{n+1} + \boldsymbol{K}_\xi{}^{n+1} + \frac{\boldsymbol{M}}{\Delta t}\right) \\ \boldsymbol{F}_{\text{eq}}{}^{n+1} &= \left(\boldsymbol{F}^{n+1} + \frac{\boldsymbol{M}}{\Delta t}\boldsymbol{T}^n\right) \end{aligned}\right\}$$
$$\Rightarrow \boldsymbol{T}^{n+1} = \left(\boldsymbol{K}_{\text{eq}}{}^{n+1}\right)^{-1}\left(\boldsymbol{F}_{\text{eq}}{}^{n+1}\right). \tag{34}$$

Δt is the time of each increment, n is the number of increments, $\boldsymbol{F}$ is the equivalent load vector, $\boldsymbol{T}$ is the temperature vector, and matrices $\boldsymbol{K}_k$, $\boldsymbol{K}_h$, $\boldsymbol{K}_\xi$, $\boldsymbol{K}_\sigma$ and $\boldsymbol{M}$ represent the heat conduction, the heat convection, the latent heat due to martensitic volume fraction variations, the latent heat due to stress

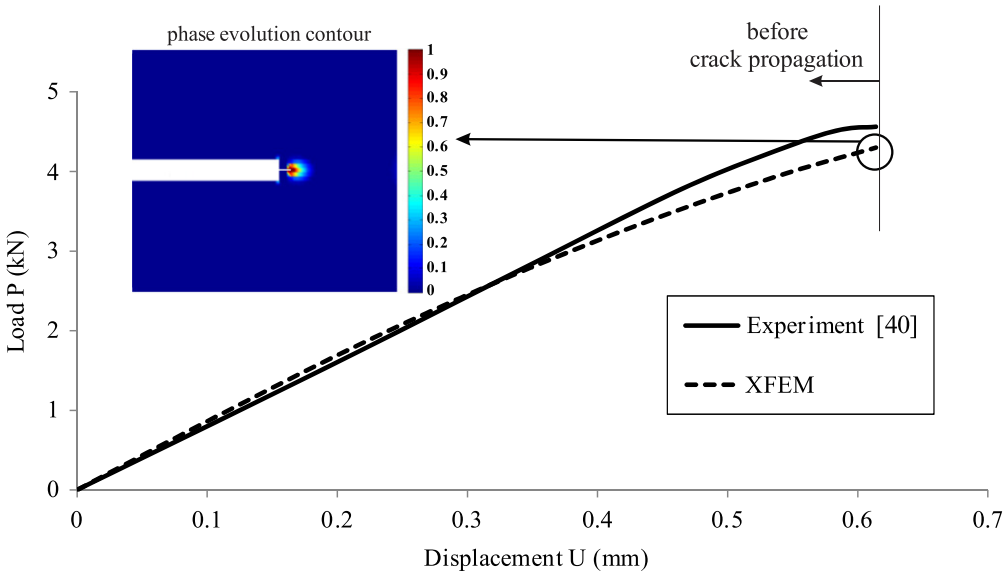

Figure 14. Force–displacement curve for the isothermal condition and before the crack propagation.

variations and heat capacity, respectively

$$
\begin{aligned}
(\boldsymbol{F})_i &= \int_S hT_{\text{ext}}\phi_i \mathrm{d}S + \int_\Omega \pi\dot{\xi}\phi_i \mathrm{d}\Omega,\\
(\boldsymbol{M})_{ij} &= \int_\Omega \rho c\phi_i\phi_j \mathrm{d}\Omega,\\
\left(\boldsymbol{K}_\xi\right)_{ij} &= \int_\Omega \rho\Delta s_0\dot{\xi}\phi_i\phi_j \mathrm{d}\Omega,\\
\left(\boldsymbol{K}_h\right)_{ij} &= \int_S h\phi_i\phi_j \mathrm{d}S,\\
\left(\boldsymbol{K}_\sigma\right)_{ij} &= \int_\Omega \boldsymbol{\alpha}\colon\dot{\boldsymbol{\sigma}}\phi_i\phi_j \mathrm{d}\Omega,\\
\left(\boldsymbol{K}_k\right)_{ij} &= \int_\Omega k\,\nabla\phi_i\,\nabla\phi_j \mathrm{d}\Omega.
\end{aligned}
\tag{35}
$$

4. Numerical issues

4.1. Selecting the enriched nodes

Figure 4 demonstrates the way different nodes are selected for enrichment with the heaviside function. In order to ensure the continuity of the displacement field between the tip element (element A) and the element ahead of the crack tip (element B), all the nodes of the split element are enriched by the heaviside function except the common nodes of these two elements.

4.2. Numerical integration

A 2×2 Gauss–Legendre quadrature rule is employed for numerical integration of the standard bilinear quadrilateral elements. For elements containing a discontinuity, the standard integration rule cannot provide accurate results, and the well-developed sub-triangle technique is adopted. Accordingly, when an element contains a discontinuity and one or some of its nodes are enriched with the heaviside function, the element is subdivided into sub-triangles and a conventional integration rule is then adopted in each triangle, as shown in figure 5. For details, see [38].

4.3. Crack propagation

The crack analysis starts with an assumed initial crack and then a crack propagation criterion is examined to determine the stability of crack and its potential propagation direction. Also, the crack is assumed to propagate as a finite straight line inside the finite element at each stages of propagation. For numerical implementation, a crack propagates when the effective stress ahead of the crack tip reaches to the critical stress σ_{crit}.

For determining the direction in which the strong discontinuity (crack) is extended, the method presented in [39] is applied. Accordingly, the crack propagates in the direction in which the effective stress $\bar{\sigma}'$ (see equation (5)) is maximum. By applying a weighted averaging of the effective stresses at all the integration points in front of a crack tip, the direction of crack propagation $\bar{\boldsymbol{d}}$ is estimated by (see figure 6)

$$
\bar{\boldsymbol{d}} = \sum_{i=1}^{n}\left(\frac{H_i^P\,\bar{\sigma}'_i\,w_i V_i}{\|\boldsymbol{d}_i\|}\boldsymbol{d}_i\right),
\tag{36}
$$

where $\boldsymbol{d}_i$ is the vector in the direction of the integration point i, n is the number of integration points, V_i is the volume related to the integration point i and H_i^P is the tip-based heaviside function

$$
H_i^P = \begin{cases} 1 & \dfrac{\boldsymbol{d}_i.\,\boldsymbol{d}_t}{\|\boldsymbol{d}_i\|\|\boldsymbol{d}_t\|} \geqslant 0,\\[2ex] 0 & \dfrac{\boldsymbol{d}_i.\,\boldsymbol{d}_t}{\|\boldsymbol{d}_i\|\|\boldsymbol{d}_t\|} < 0, \end{cases}
\tag{37}
$$

where $\boldsymbol{d}_t$ is the vector tangential to the crack at its tip. The

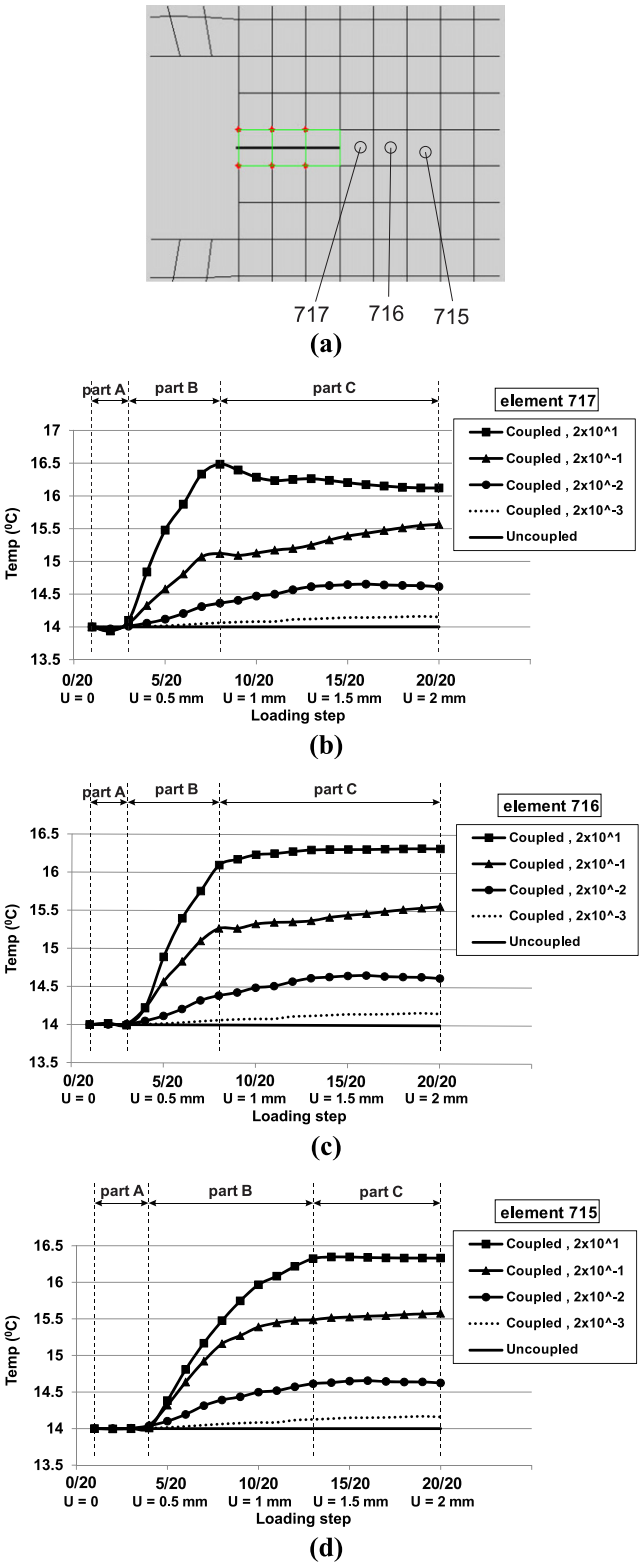

Figure 15. Temperature in crack tip elements (a) definition of crack tip elements, (b) element 717, (c) element 716, (d) element 715.

heaviside function H_i^P is included in the weighted averaging (36) to ensure that only the Gauss points ahead of the crack tip are included.

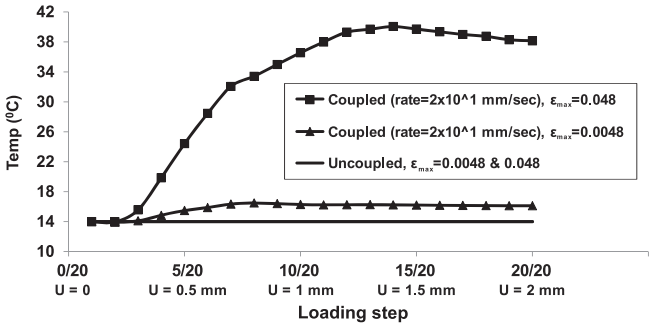

Figure 16. Effect of transformation strain on the temperature of crack tip element (element 717).

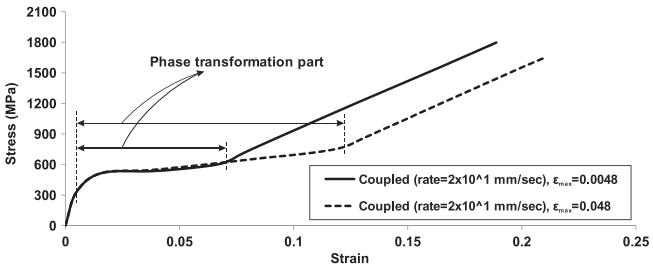

Figure 17. Local strain–stress curve in the crack tip element for two transformation strains of 0.0048 and 0.048 (element 717).

In equation (36), w_i is a Gaussian weighting function related to the ith integration point [39]

$$w_i = \frac{\exp\left(-\dfrac{\|\boldsymbol{d}_i\|^2}{2l^2}\right)}{l^3(2\pi)^{3/2}}, \tag{38}$$

where l is the length parameter which is considered 2–3 times bigger than the average size of the elements ahead of the crack tip.

5. Numerical simulations

5.1. A square plate with a central crack under mode I loading

In order to verify the proposed approach, a central crack square plate with the crack length to the plate width ratio of $a/W = 0.05$, is simulated under the mode I loading condition and the plane stress state. The initial ambient temperature is equal to 25 °C. First, this problem is simulated with a slow loading rate (isothermal condition) and the results are compared with the available analytical and numerical results [10]. Then, a simulation with high loading rate is carried out and the results are compared with the ones obtained in the slow loading rate. Considering the symmetry in geometry and loading conditions, only half of the geometry is modeled with appropriate boundary conditions. Finer elements are used around the crack tip, to allow for better capturing of stress concentration and better prediction of the nonlinear behavior of the elements due to the phase transformation. Accordingly,

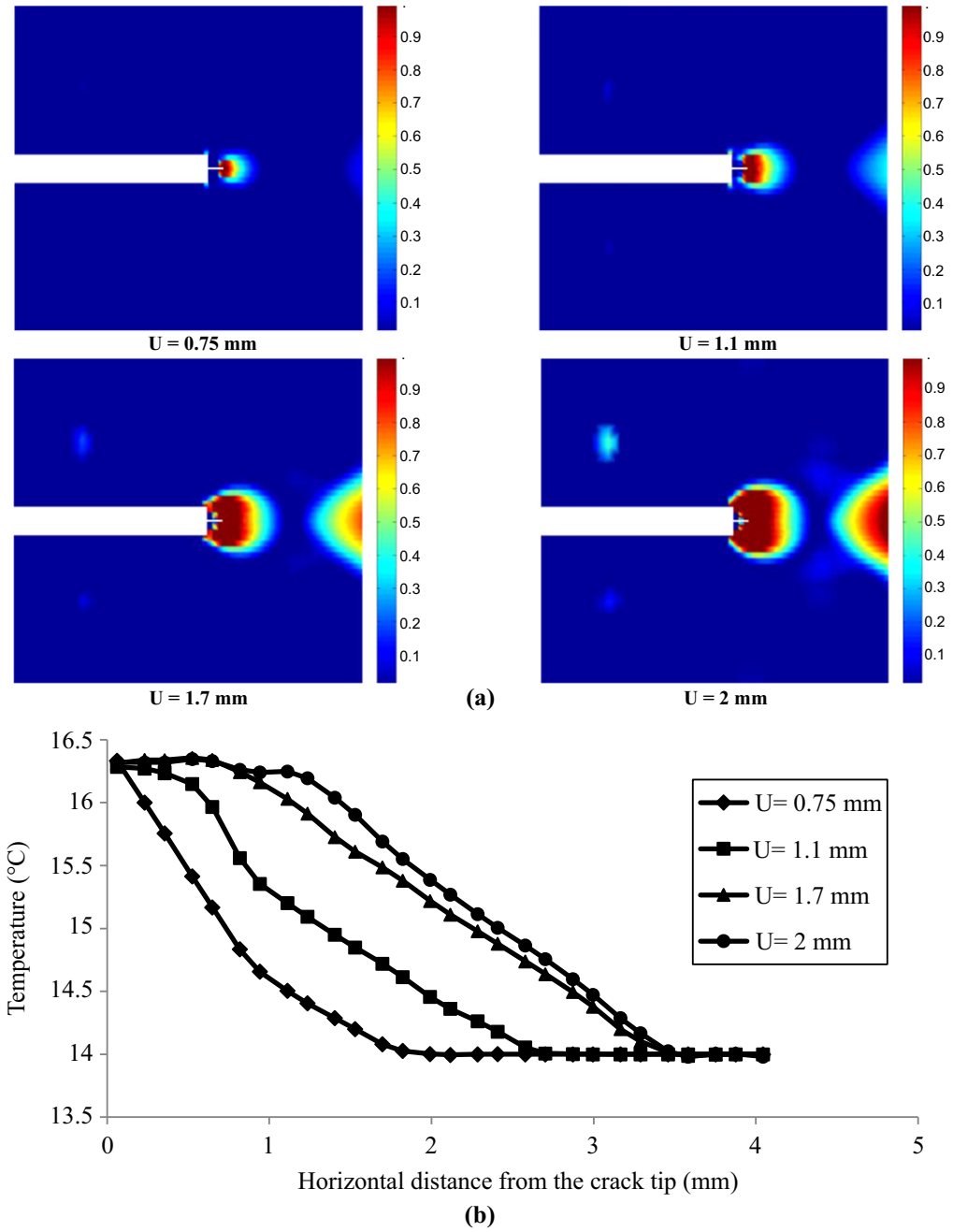

Figure 18. Phase evolution contour and temperature distribution at the loading rate of $2 \times 10^{+1}$ mm s^{-1} (a) phase evolution contour, (b) temperature distribution.

about 4500 bilinear quadrilateral elements are used to discretize the domain, as shown in figure 7.

The basic material properties are listed in table 1. Based on the assumptions of the reference [10], this problem is simulated by assuming that σ_{M_s} is equal to σ_{M_f}, called the transformation stress σ^{tr} $\left(\sigma^{tr} = \sigma_{M_s} = \sigma_{M_f}\right)$. Using the linear transformation surfaces in the constitutive model of Lagoudas [1] and the transformation stress (σ^{tr}), the critical temperatures of the phase transformation (A_f, A_s, $M_s$and M_f) can be calculated. Therefore, for two transformation stresses $\sigma^{tr} = 100$ 200 MPa, which are related to two different materials, the values of A_f, A_s, $M_s$and M_f are listed in table 1. Several simulations are performed by changing the thermodynamics characteristics of the material, such as the transformation stress (σ^{tr}) and the maximum strain due to the phase transformation (ε_{max}), to allow for a comprehensive investigation of the phase transformation effects around the crack tip.

Figure 8 presents a comparison between the results of proposed extended finite element model and the analytical and numerical (FE analysis) models by Maletta and Furgiuele [10] in prediction of von Mises stress in the horizontal direction from the crack tip. These results are related to the case in which the remote tensile stress of the

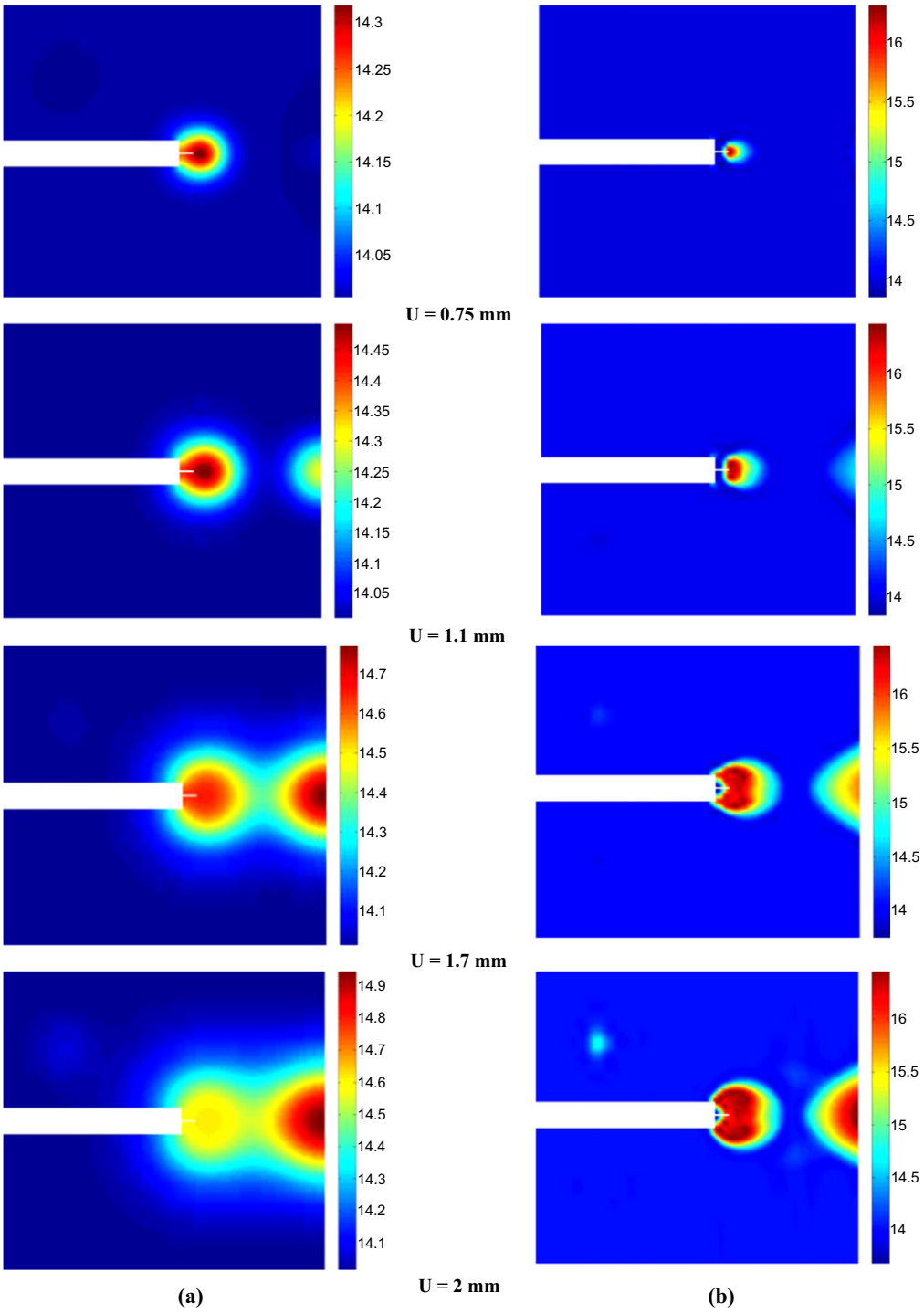

Figure 19. Temperature distribution contours for slow and high loading rates (a) slow loading rate $\left(2 \times 10^{-2}\ \text{mm s}^{-1}\right)$, (b) high loading rate $\left(2 \times 10^{+1}\ \text{mm s}^{-1}\right)$.

plate (σ^{∞}) is 62.5 MPa and the loading rate is slow. Clearly, the XFEM results in three regions of A, $A \rightarrow M$ and M are in a good agreement with the reference analytical and finite element results. Also the number of elements in the XFEM analysis (4500 elements) is decreased to half compared to the reference FE analysis (9500 elements) and unlike the FE analysis the crack is not geometrically modeled.

Now, by changing the main thermo-mechanical characteristics of the alloy, i.e. the transformation strain $\varepsilon_{\max}$ and transformation stress σ^{tr}, a series of simulations are carried out. Figures 9(a) and (b) compare the size of the phase transformation regions in terms of distances r_A and r_M (schematically shown in figure 2), for the proposed extended finite element model and the reference of analytical and finite element models [10] under the remote tensile stress

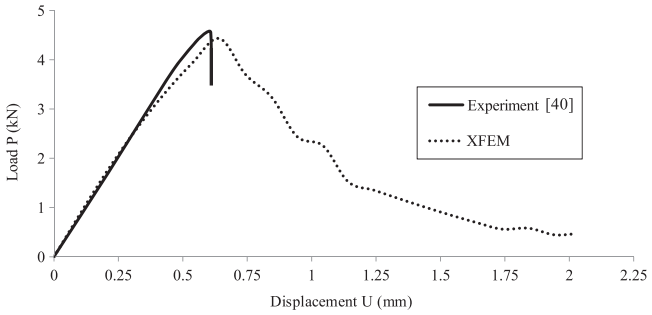

Figure 20. Force–displacement curve for the isothermal case.

$\sigma^{\infty} = 62.5$ MPa with a slow loading rate. Figures 9(a) and (b) demonstrate that the obtained results have a good agreement with the analytical and FEM results [10], while substantially reducing the number of elements from the reference 9500 to present 4500 elements. Figure 9(c) illustrates the phase evolution contour in the crack tip for $\sigma^{\infty} = 62.5$ MPa and $\varepsilon_{\max} = 1\%$. It is observed that in the region near to the crack tip, the phase is martensite (M), and a little far from the crack tip, the phase transformation ($A \rightarrow M$) occurs, while further away from this region no phase transformation happens and the material remains in the austenite (A) phase.

Now, the effects of loading rate on the von Mises stress around the crack tip and the size of phase transformation regions are investigated. Figure 10 compares the von Mises stress in the horizontal direction from the crack tip for the two cases of slow and high loading rates. It is observed that in the case of high loading rate, variations of the stress around the crack tip do not remain constant (and equal to σ^{tr}) in the phase transformation region and show a decreasing trend. As a result of the thermo-mechanical coupling, the stress depends directly to the heat, meaning that it increases by the release of heat. Since noticeable amount of heat is released in the case of high loading rate, the stress is also increased in the phase transformation region ($A \rightarrow M$) and the material shows a hardening behavior (see figure 11), with a varying value for the von Mises stress in the phase transformation region (see figure 10).

Figure 12 illustrates a comparison between the sizes r_A and r_M of the phase transformation regions for two cases of slow and high loading rates with $\sigma^{\mathrm{tr}} = 200$ MPa. As can be observed in the case of high loading rate, the sizes of r_A and r_M are considerably decreased in comparison with the slow loading rate. The reason for this phenomenon is that the phase transformation in the case of slow loading rate is completed in a lower level of strain compared with the case of high loading rate ($\varepsilon_{\mathrm{H}} > \varepsilon_{\mathrm{S}}$ in figure 11) and therefore r_A and r_M zones have sufficient time for growth. Hence, the size of r_A and r_M become smaller in the case of high loading rate.

5.2. Compact tension test with the thermo–mechanical coupling effects

In this example, a compact-tension specimen with a notch is numerically simulated. Geometry and dimensions of the experimental model [40] are presented in figure 13(a). A finite element mesh with bilinear quadrilateral elements is used to discretize the domain, as shown in figure 13(b). In this test, an initial crack with $a/W = 0.504$ is assumed in the problem and the force P is inserted in two opposite directions in the points B_1 and B_2 (see figure 13(a)). This geometry and loading lead to crack propagation in mode I. The specimen has the thickness of 8 mm and it is analyzed in the plane stress state. The initial ambient temperature is equal to 14 °C. The other required characteristics are presented in table 2.

First, the problem is analyzed under the isothermal condition and the obtained results are compared with the experimental ones. Then, in order to observe the thermal concentration in the crack tip, the problem is simulated with different loading rates, which are presented in table 3.

5.2.1. Stationary crack. In this section, it is assumed that no crack propagation occurs in the domain. First, the problem is verified for isothermal conditions and then the effect of different loading rates on material behavior is examined. Figure 14 presents the force–displacement P–U curve for the isothermal condition and before the crack propagation in the domain. U represents the relative vertical displacement of points A_1 and A_2. It can be observed that the numerical and reference experimental results [40] are in a good agreement. Also, it can be seen that the material behavior is linear elastic at the start of loading and by increasing the load, the phase transformation occurs around the crack tip.

Evaluation of the temperature variations in the crack tip elements for different loading rates. Figure 15 depicts the effect of loading rate on temperature of three elements in front of the crack tip. It is observed that as the loading rate is decreased, the temperature in crack tip elements is decreased to the ambient temperature (14 °C—isothermal condition). Three parts are observable in all curves of figure 15. The first part (part A) is related to the linear elastic behavior where the temperature of all elements is equal to the ambient temperature for all loading rates (heat is not released yet).

In the second part (part B), the temperature in the crack tip elements is increased by the time of loading. In this region, the phase transformation is started and the heat is also released. At the end of this part, the forward phase transformation process is completed.

The third part (part C) is related to the case in which the forward phase transformation is completed and the heat transfer phenomenon may lead to increase or decrease of temperature, with no predictable trend for the temperature in this part.

In figure 15, it is observed that the temperature of the crack tip elements can only be increased up to 2.5 °C in the highest loading rate, which is in agreement with recent infrared thermography measurements [41]. Furthermore, if this problem is solved with a larger transformation strain, the temperature of the crack tip element is remarkably increased. In figure 16, the effect of transformation strain on behavior of the crack tip element is demonstrated. Now, by considering $\varepsilon_{\max} = 0.048$, the temperature of the crack tip element

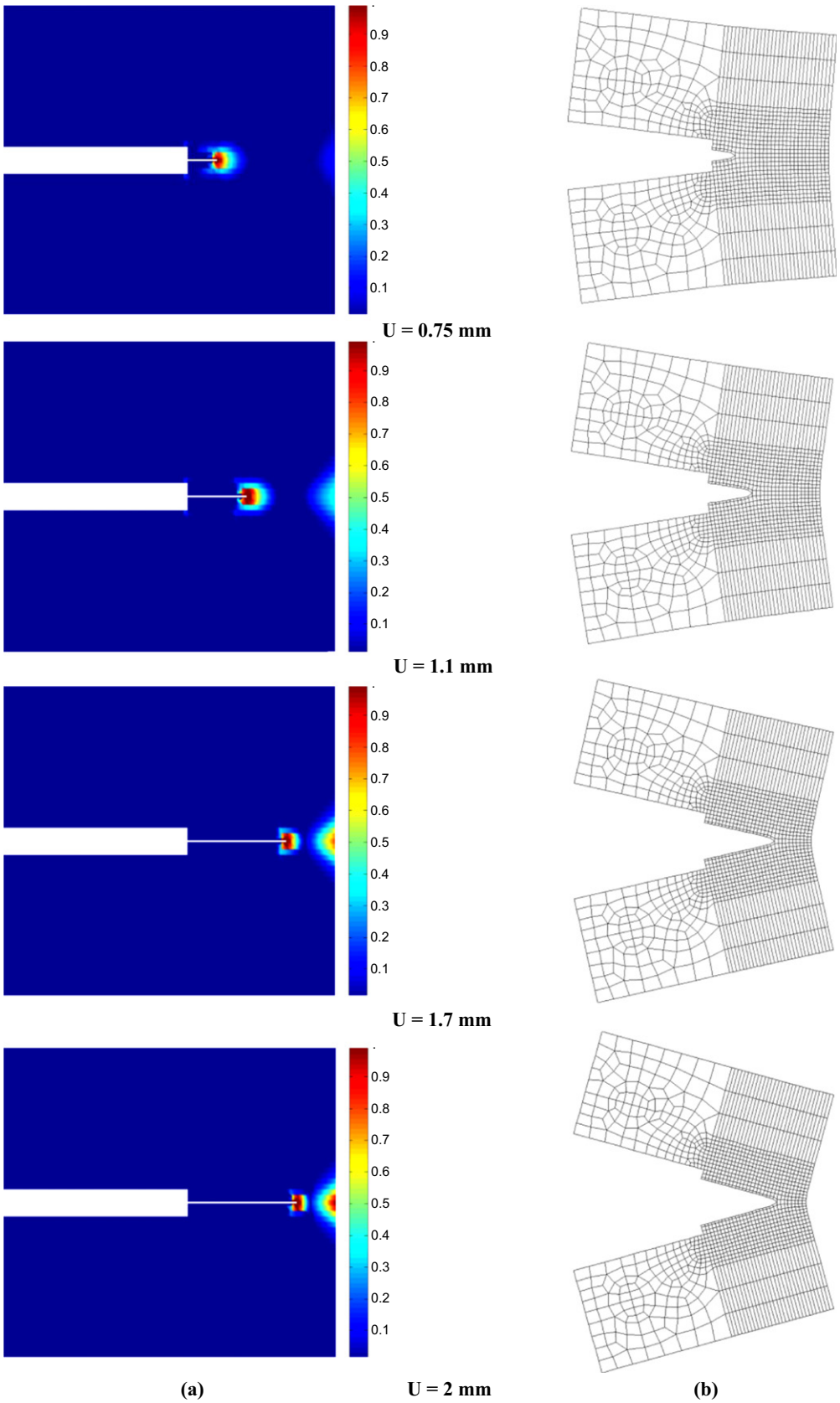

Figure 21. Phase evolution and shape deformation for the isothermal case (a) phase evolution, (b) deformed shape (magnified by ×5).

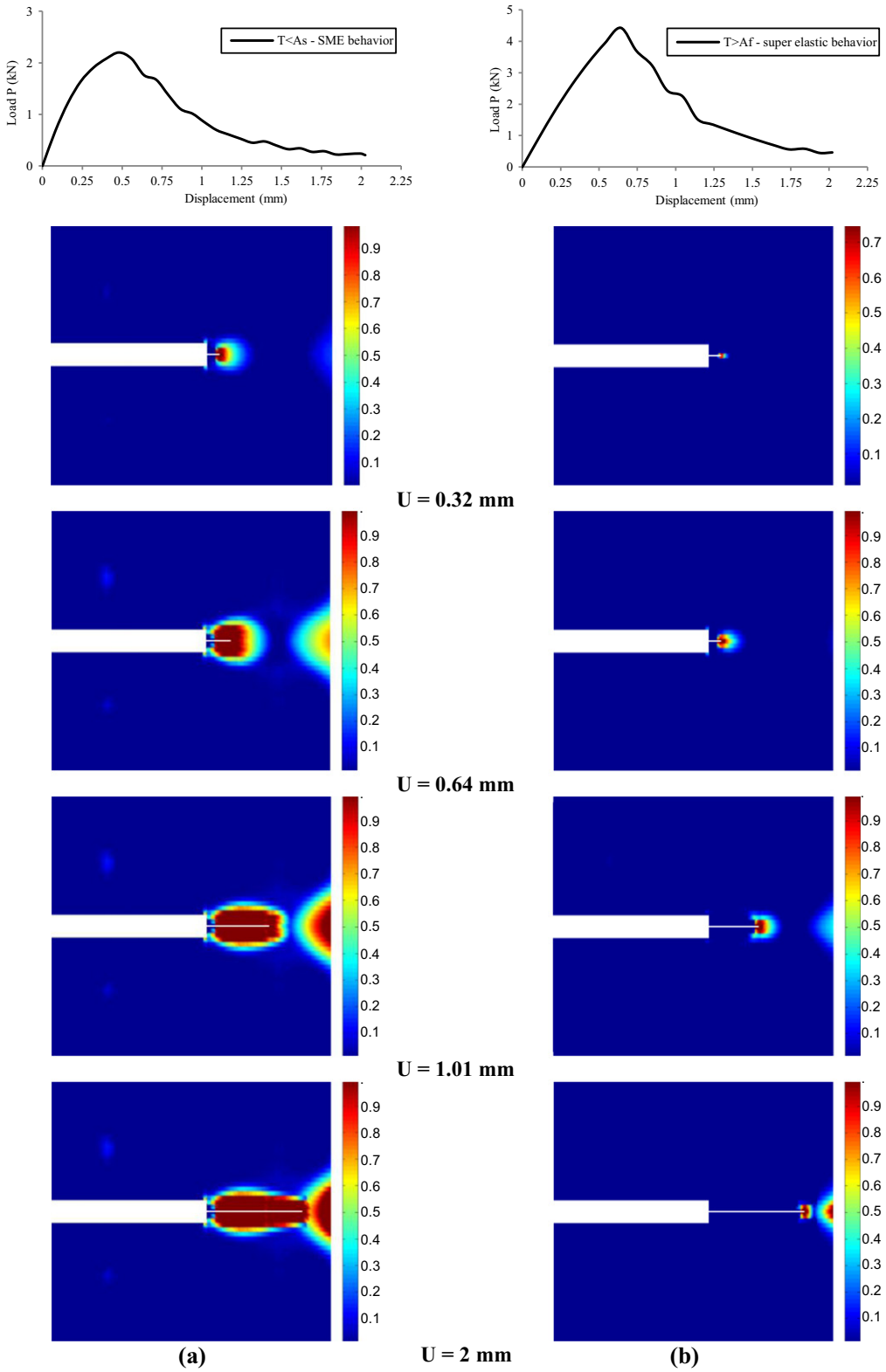

Figure 22. Phase evolution contours for two cases of ambient temperature (a) $T < A_s$ (SME behavior), (b) $T > A_f$ (super elastic behavior).

becomes remarkably higher than the case of $\varepsilon_{max} = 0.0048$. The local strain–stress curve in the crack tip element (element 717) is depicted in figure 17, which shows that for the case of $\varepsilon_{max} = 0.048$, the length of the phase transformation part is larger than the case of $\varepsilon_{max} = 0.0048$; meaning that the material has more time for phase transformation. In addition, considering that the heat is only released in the phase transformation part, thus the temperature of the crack tip element in this case becomes higher than the case of $\varepsilon_{max} = 0.0048$.

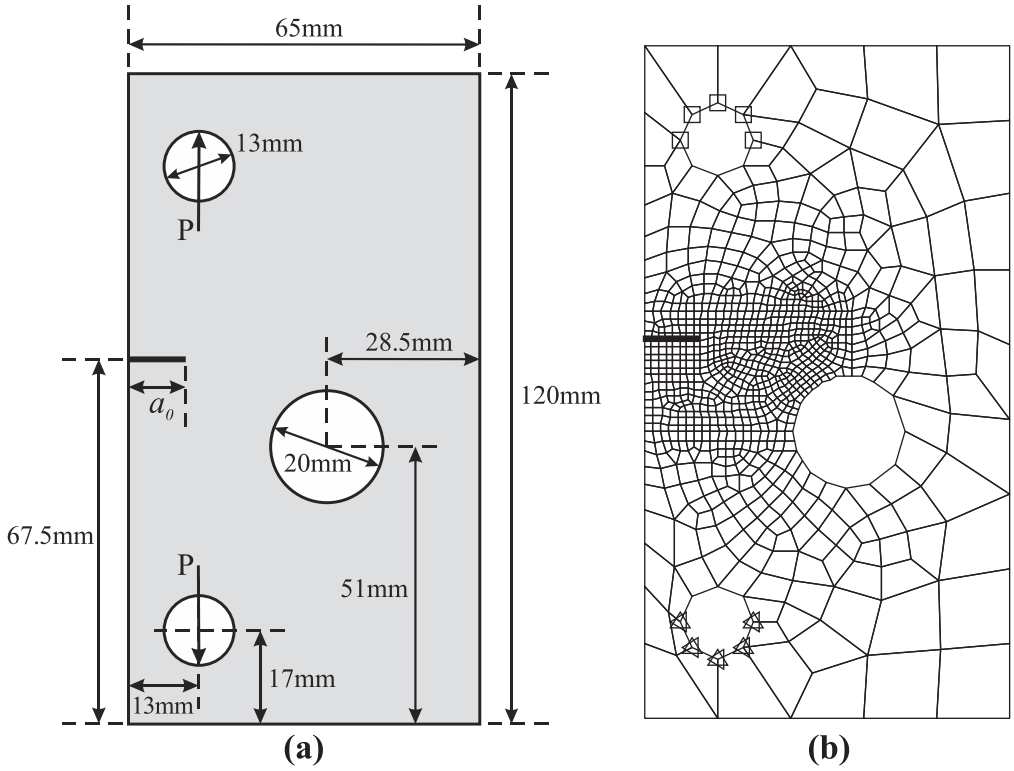

Figure 23. Geometric details of the cracked plate with holes.

Table 4. Material properties of the SMA plate with holes.

E_A	52×10^9 Pa	$C_A = C_M$	10×10^6 Pa K^{-1}
E_M	52×10^9 Pa	ε_{max}	0.032
$\nu_A = \nu_M$	0.33	k	18.3 W (mK)$^{-1}$
M_s	−11 °C	h_{Air}	4 W (m^{2}K)$^{-1}$
M_f	−11.1 °C	$(\sigma_{crit})_{super\ elastic}$	600 MPa
A_s	3 °C	$(\sigma_{crit})_{SME}$	300 MPa
A_f	5.5 °C		

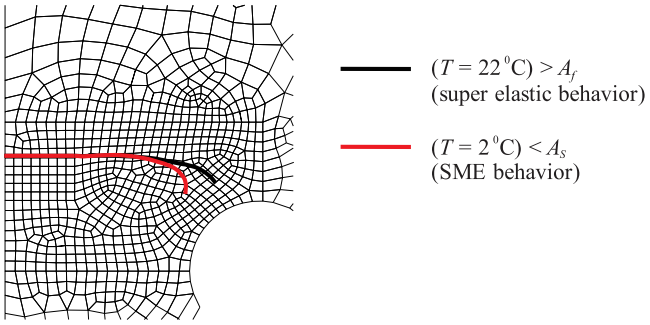

Figure 24. Crack tracks obtained from two cases of ambient temperature (T = 2,22 °C).

Phase evolution and temperature distribution contours in the case of high loading rate $\left(2 \times 10^{+1}\ \text{mm s}^{-1}\right)$. In figure 18, the phase evolution contour and temperature distribution in the crack tip are depicted for different stages of loading. It can be observed that by starting the phase transformation in the crack tip, the heat is released and therefore the temperature in the crack tip is increased. Also, with the growth of phase transformation zone, the temperature changes in a larger zone. These results are obtained for the loading rate of $2 \times 10^{+1}$ mm s^{-1} and the transformation strain of 0.0048.

Evaluation of temperature distribution contours for slow and high loading rates $\left(2 \times 10^{-2}\ \text{mm s}^{-1},\ 2 \times 10^{+1}\ \text{mm s}^{-1}\right)$. Figure 19 illustrates the temperature distribution contours for slow and high loading rates in different stages of loading. These results are obtained for the transformation strain of 0.0048. Clearly, for a slow loading rate, the temperature distribution occurs in a larger zone (the radius of temperature circles are bigger around the crack tip). The reason can be attributed to the fact that the material has more time for heat transfer to the surrounding parts.

5.2.2. Crack propagation. In this section, the experimental test presented in [40] is analyzed under the isothermal condition. Figure 20 demonstrates the force–displacement curves for present numerical results and the reference experimental data [40]. The experiments in reference [40] were carried out under the force-control conditions, which was not capable of measuring the softening part of the curve. Therefore, the reference results [40] are only available up to the peak of loading capacity (before crack propagation). Clearly, in the present XFEM analysis, the force–displacement response can be obtained even for the crack propagation part where the loading capacity of structure is decreased.

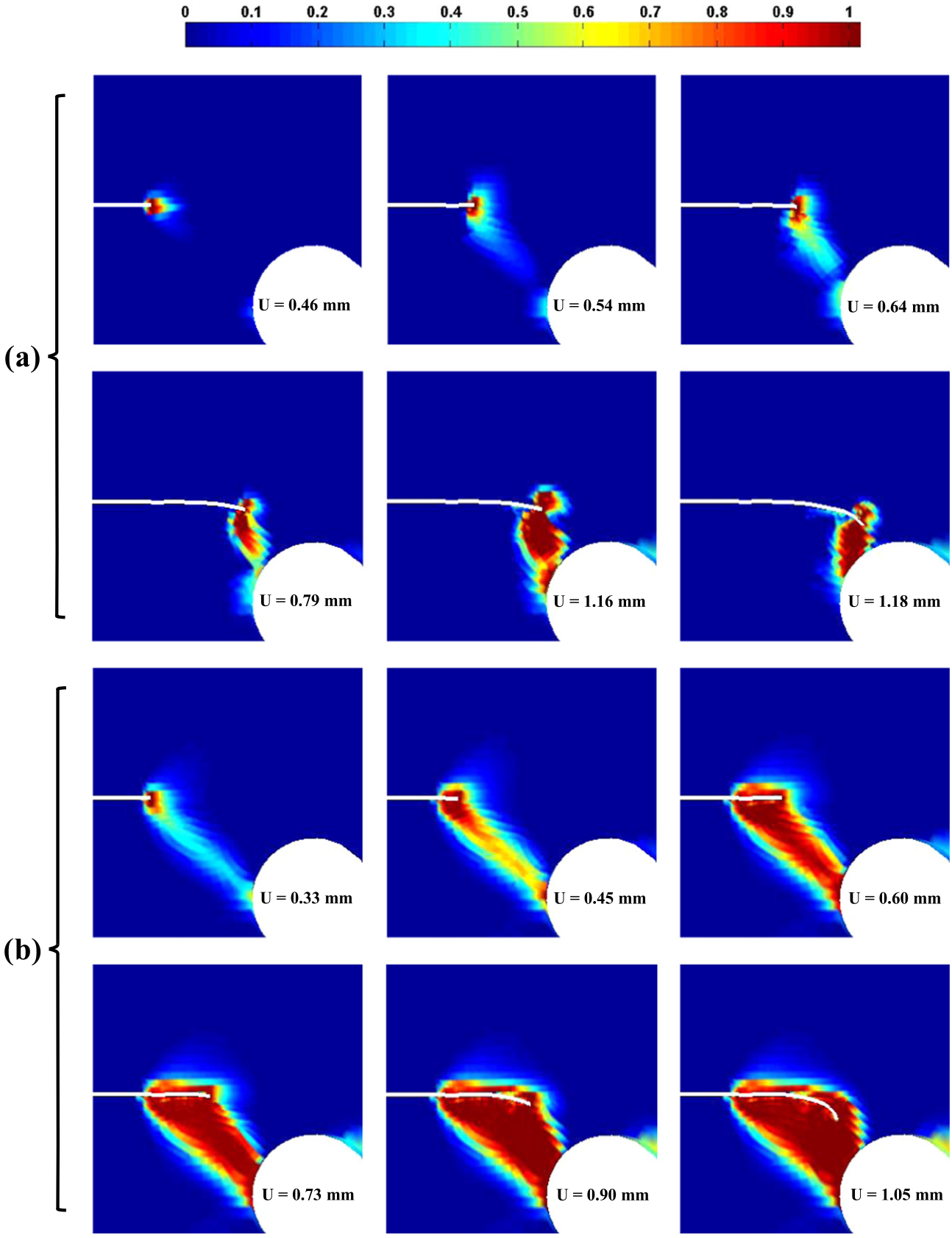

Figure 25. Phase evolution contours for two cases of ambient temperature (a) $T > A_f$ (super elastic behavior), (b) $T < A_s$ (SME behavior).

The phase evolution and shape deformation contours in different stages of loading are depicted in figure 21. By increasing the loading steps, the phase transformation region in the crack tip is grown. Then, crack propagates in the mode I according to the criterion for crack propagation. Also, it can be observed that the phase evolution is always concentrated in the crack tip, and the reverse phase transformation occurs on crack surface (the martensitic phase transforms to the austenitic phase).

5.2.3. Effect of the ambient temperature on SMA behavior.

Assuming an isothermal condition, the effect of ambient temperature (T) on SMA behavior is investigated in this section. Considering the Lagoudas model for SMA [1], if the ambient temperature is less than A_s, the forward phase transformation occurs in loading and the reverse phase transformation does not occur in unloading, so the material is elastically unloaded similar to a plastic material (SME). The reason for this phenomenon is that the austenitic phase is not a stable phase in this temperature. Therefore, if $T > A_f$ (see figure 1), the material has the super elastic behavior while for $T < A_s$, the behavior is SME and there will be residual strains after unloading. In this example, A_s is equal to -8.5 °C, and in order to have the super elastic behavior, the ambient temperature is considered 14 °C (the ambient temperature in previous sections of this example was 14 °C). While the SME behavior is activated by the ambient temperature of -15 °C. These two cases ($T > A_f$ and $T < A_s$) are compared in this section.

In figure 22, phase evolution contours for two cases of material behavior in the different stages of loading are depicted. It can be observed that if the material has the super elastic behavior, the phase evolution is concentrated around the propagating crack tip and the reverse phase transformation occurs on crack surfaces. On the other hand, if the material has the SME behavior, the reverse phase transformation does not occur on crack surfaces and there will be residual strains after unloading.

5.3. Crack propagation in a plate with holes

In this example, a plate with three holes is numerically simulated. Geometry and dimensions of the model are presented in figure 23(a). The original numerical and experimental test of this problem was performed on aluminum in [42], and it is now changed to SMA to discuss the proposed approach for dealing with the complex case of mixed mode crack propagation. An initial crack with $a = 10$ mm is assumed which is located slightly above the center of plate. In order to prevent rigid body motions, the displacement is fixed in the bottom hole in the x and y directions; and the y-displacement loading is imposed on the top hole. A finite element mesh with bilinear quadrilateral elements is used to discretize the domain, as shown in figure 23(b). Two values are considered for the initial ambient temperature ($(T = 2\ °C) < A_s$ and $(T = 22\ °C) > A_f$). It will be observed that for $(T = 22\ °C) > A_f$ and $(T = 2\ °C) < A_s$, the behaviors become super elastic and SME, respectively. The required material properties are presented in table 4.

Figure 24 illustrates the crack paths obtained from two cases of ambient temperature ($T = 2,\ 22$ °C). It is observed that the crack paths are identical at the beginning of crack propagation, and they become different when the crack tip locates close to the hole. The reason of this difference is that the material behavior in the crack tip is not the same for two cases of temperature. In figure 25, phase evolution contours for two cases of ambient temperature in the different stages of loading are depicted. It can be observed that for $T > A_f$ (super elastic behavior), the reverse phase transformation occurs on crack surfaces in different stages of loading, while for $T < A_s$ (SME behavior), the reverse phase transformation does not occur on crack surfaces.

6. Conclusion

Fracture of SMAs has been analyzed by using XFEM and considering the coupling effects. The heaviside enrichment function has been employed for modeling of the discontinuities in the finite element mesh, and any crack propagation problem can be modeled without remeshing. It has been illustrated that the stress field, temperature and size of the phase transformation regions in the crack tip have strong dependency to the loading rate. As a result, considering the effects of thermo-mechanical coupling is very important in fracture analysis of SMAs. Also, it has been observed that if the material has the super elastic behavior, the phase evolution and von Mises strain are concentrated around the propagating crack tip and the reverse phase transformation occurs on crack surfaces. On the other hand, if the material has the SME behavior, the reverse phase transformation does not occur on crack surfaces and residual strains remain after unloading. Finally, in order to demonstrate the capabilities of the proposed method in more complicated SMA problems, a mixed mode crack propagation problem has been simulated and comprehensively discussed.

Acknowledgments

The authors wish to acknowledge the technical support of the High Performance Computing Lab, School of Civil Engineering, University of Tehran. The financial support of Iran National Science Foundation (INSF) is gratefully acknowledged.

References

[1] Lagoudas D C 2008 *Shape Memory Alloys: Modeling and Engineering Applications* (New-York: Springer)
[2] Freed Y and Banks-Sills L 2007 Crack growth resistance of shape memory alloys by means of a cohesive zone model *J. Mech. Phys. Solids* **55** 2157–80

[3] Qidwai M A and Lagoudas D C 2000 Numerical implementation of a shape memory alloy thermomechanical constitutive model using return mapping algorithms *Int. J. Numer. Methods Eng.* **47** 1123–68

[4] Gollerthan S, Herberg D, Baruj A and Eggeler G 2008 Compact tension testing of martensitic/pseudoplastic NiTi shape memory alloys *Mater. Sci. Eng.* A **481** 156–9

[5] Gollerthan S, Young M L, Baruj A, Frenzel J, Schmahl W W and Eggeler G 2009 Fracture mechanics and microstructure in NiTi shape memory alloys *Acta Mater.* **57** 1015–25

[6] Gollerthan S, Young M L, Neuking K, Ramamurty U and Eggeler G 2009 Direct physical evidence for the back-transformation of stress-induced martensite in the vicinity of cracks in pseudoelastic NiTi shape memory alloys *Acta Mater.* **57** 5892–7

[7] Robertson S W, Mehta A, Pelton A R and Ritchie R O 2007 Evolution of crack-tip transformation zones in superelastic nitinol subjected to *in situ* fatigue: a fracture mechanics and synchrotron x-ray microdiffraction analysis *Acta Mater.* **55** 6198–207

[8] Birman V 1998 On mode I fracture of shape memory alloy plates *Smart Mater. Struct.* **7** 433

[9] Desindes S and Daly S 2010 The small-scale yielding of shape memory alloys under mode III fracture *Int. J. Solids Struct.* **47** 730–7

[10] Maletta C and Furgiuele F 2010 Analytical modeling of stress-induced martensitic transformation in the crack tip region of nickel–titanium alloys *Acta Mater.* **58** 92–101

[11] Yi S and Gao S 2000 Fracture toughening mechanism of shape memory alloys due to martensite transformation *Int. J. Solids Struct.* **37** 5315–27

[12] Maletta C 2012 A novel fracture mechanics approach for shape memory alloys with trilinear stress–strain behavior *Int. J. Fract.* **177** 39–51

[13] Wang G Z 2006 Effects of notch geometry on stress–strain distribution, martensite transformation and fracture behavior in shape memory alloy NiTi *Mater. Sci. Eng.* A **434** 269–79

[14] Wang G Z 2007 A finite element analysis of evolution of stress–strain and martensite transformation in front of a notch in shape memory alloy NiTi *Mater. Sci. Eng.* A **460** 383–91

[15] Wang G Z, Xuan F Z, Tu S T and Wang Z D 2010 Effects of triaxial stress on martensite transformation, stress–strain and failure behavior in front of crack tips in shape memory alloy NiTi *Mater. Sci. Eng.* A **527** 1529–36

[16] Baxevanis T and Lagoudas D C 2012 A mode I fracture analysis of a center-cracked infinite shape memory alloy plate under plane stress *Int. J. Fract.* **175** 151–66

[17] Baxevanis T, Parrinello A F and Lagoudas D C 2013 On the fracture toughness enhancement due to stress-induced phase transformation in shape memory alloys *Int. J. Plast.* **50** 158–69

[18] Belytschko T, Lu Y Y and Gu L 1994 Element-free Galerkin methods *Int. J. Numer. Methods Eng.* **37** 229–56

[19] Cruse T A 1988 *Boundary Element Analysis in Computational Fracture Mechanics* vol 1 (The Netherlands Dordrecht: Kluwer, Springer)

[20] Rabczuk T and Belytschko T 2004 Cracking particles: a simplified meshfree method for arbitrary evolving cracks *Int. J. Numer. Methods Eng.* **61** 2316–43

[21] Belytschko T and Black T 1999 Elastic crack growth in finite elements with minimal remeshing *Int. J. Numer. Methods Eng.* **45** 601–20

[22] Daneshyar A and Mohammadi S 2013 Strong tangential discontinuity modeling of shear bands using the extended finite element method *Comput. Mech.* **52** 1023–38

[23] Samaniego E and Belytschko T 2005 Continuum–discontinuum modelling of shear bands *Int. J. Numer. Methods Eng.* **62** 1857–72

[24] Bayesteh H and Mohammadi S 2013 XFEM fracture analysis of orthotropic functionally graded materials *Composites* B **44** 8–25

[25] Dolbow J and Gosz M 2002 On the computation of mixed-mode stress intensity factors in functionally graded materials *Int. J. Solids Struct.* **39** 2557–74

[26] Hosseini S, Bayesteh H and Mohammadi S 2013 Thermo-mechanical XFEM crack propagation analysis of functionally graded materials *Mater. Sci. Eng.* A **561** 285–302

[27] Mariani S and Perego U 2003 Extended finite element method for quasi-brittle fracture *Int. J. Numer. Methods Eng.* **58** 103–26

[28] Patzák B and Jirásek M 2003 Process zone resolution by extended finite elements *Eng. Fract. Mech.* **70** 957–77

[29] Elguedj T, Gravouil A and Combescure A 2006 Appropriate extended functions for X-FEM simulation of plastic fracture mechanics *Comput. Methods Appl. Mech. Eng.* **195** 501–15

[30] Seabra M R R, de Sa J M A C, Andrade F X C and Pires F F M A 2011 Continuous–discontinuous formulation for ductile fracture *Int. J. Mater. Form.* **4** 271–81

[31] Asadpoure A and Mohammadi S 2007 Developing new enrichment functions for crack simulation in orthotropic media by the extended finite element method *Int. J. Numer. Methods Eng.* **69** 2150–72

[32] Asadpoure A, Mohammadi S and Vafai A 2006 Crack analysis in orthotropic media using the extended finite element method *Thin-Walled Struct.* **44** 1031–8

[33] Esna Ashari S and Mohammadi S 2011 Delamination analysis of composites by new orthotropic bimaterial extended finite element method *Int. J. Numer. Methods Eng.* **86** 1507–43

[34] Motamedi D and Mohammadi S 2010 Dynamic crack propagation analysis of orthotropic media by the extended finite element method *Int. J. Fract.* **161** 21–39

[35] Ahmadian H, Hatefi Ardakani S and Mohammadi S 2014 Strain-rate sensitivity of unstable localized phase transformation phenomenon in shape memory alloys using a non-local model (submitted paper)

[36] Boyd J G and Lagoudas D C 1996 A thermodynamical constitutive model for shape memory materials: I. The monolithic shape memory alloy *Int. J. Plast.* **12** 805–42

[37] Moës N, Dolbow J and Belytschko T 1999 A finite element method for crack growth without remeshing *Int. J. Numer. Methods Eng.* **46** 131–50

[38] Mohammadi S 2008 *Extended Finite Element Method: for Fracture Analysis of Structures* (UK: Wiley-Blackwell)

[39] Wells G N, Sluys L J and de Borst R 2002 Simulating the propagation of displacement discontinuities in a regularized strain-softening medium *Int. J. Numer. Methods Eng.* **53** 1235–56

[40] Wang X, Xu B, Yue Z and Tong X 2008 Fracture behavior of the compact tension specimens in NiTi shape memory alloys *Mater. Sci. Eng.* A **485** 14–9

[41] Maletta C, Bruno L, Corigliano P, Crupi V and Guglielmino E 2014 Crack-tip thermal and mechanical hysteresis in shape memory alloys under fatigue loading *Mater. Sci. Eng.* A **616** 281–7

[42] Giner E, Sukumar N, Tarancon J E and Fuenmayor F J 2009 An Abaqus implementation of the extended finite element method *Eng. Fract. Mech.* **76** 347–68